The current issue and full text archive of this journal is available at
www.emeraldinsight.com/0961-5539.htm

Received 13 January 2009
Revised 24 June 2009
Accepted 30 September 2009

Numerical performance analysis of an annular miniature gas turbine power system using fuels with low heating values

Chun-Hsiang Yang, Di-Han Wu and Chiun-Hsun Chen
Department of Mechanical Engineering, National Chiao Tung University, Hsinchu, Taiwan

Abstract

Purpose – Utilizing renewable energy and developing new energy sources are practical responses to the shortage of fossil fuels and environmental regulations for carbon dioxide emissions. The purpose of this paper is to assess the practicability of using low heating value (LHV) fuel on an annular miniature gas turbine (MGT) via numerical simulations.

Design/methodology/approach – The MGT used in this study is MW-44 Mark I, whose original fuel is liquid (Jet A1). Its fuel supply system is re-designed to use biogas fuel with LHV. The simulations, aided by the commercial code CFD-ACE+, were carried out to investigate the cooling effect in a perforated combustion chamber and combustion behavior in an annular MGT when using LHV gas. In this study, four parameters of rotational speeds are considered. At each specific speed, various mixture ratios of methane (CH_4) to carbon dioxide (CO_2) including 90, 80, 70, and 60 percent were taken into consideration as simulated LHV fuels.

Findings – The simulation results show the chamber design can create a proper recirculation zone to concentrate the flame at the center of the chamber, and prevent the flame from expanding to cause hot spot. Furthermore, the hot gas exhausted from combustor outlet is cooled down effectively by jet flow discharged from dilution holes, which prevent turbine blade from heat damage.

Originality/value – Simulation results demonstrate that CFD-ACE+ can simulate flow field performance and combustion behavior in an annular MGT precisely. The results of these CFD analyses confirm that the methane fuel can be used in such small volume of MGT and still have high performance. With the aid of the constructed combustor model, the performance of a methane-used MGT can be realized before the experiment procedure starts.

Keywords Natural gas, Turbines, Fuels, Combustion chambers
Paper type Research paper

Nomenclature

C_p	constant pressure specific heat
D_h	hydraulic diameter
Ea	activation energy
h	total enthalpy
I	turbulence intensity
k	k-equation for turbulent model
k_t	thermal conductivity
k_r	reaction rate constant
$\dot{m}$	mass flow rate
M_i	molecular weight
p	pressure
Pr	Prandtl number
R	ideal gas constant
R_u	universal gas constant
s_{ij}	rate of strain tensor
S_h	energy source
Sc	Schmidt number
T	temperature
u, v, w	velocity components in the (x, y, z) system of coordinates
u_i	velocity component
$\vec{V}$	velocity vector

International Journal of Numerical Methods for Heat & Fluid Flow
Vol. 20 No. 7, 2010
pp. 794-810

0961-5539
DOI 10.1108/09615531011065575

x_i Cartesian coordinate (i = 1, 2, 3)

Y_i mass fraction

τ_{ij} stress tensor component

μ viscosity

ρ density

η efficiency

ε dissipation rate

1. Introduction

The utilization of renewable energy and development of new energy sources are government policy. Since a large amount of marsh gas derived from wastes is an optimal resource at present, the use of methane fuel to activate a miniature gas turbine (MGT) engine has been widely discussed. Such distributed power supply system is small, low cost, easy to maintain and suited to household use. Much previous research on MGT had made effort to improve the combustor efficiency or to bring up novel designs. Most design factors and coefficients were obtained from experiments and designers' experience. Especially, the combustion chamber is the most heavily thermal load part in a turbine engine and its service life is normally very short. Since very limited data can be obtained from expensive engine tests due to its serious work environment, a well founded numerical simulation will lower the process cost between design and experiment layout.

In a recent study, Gulati *et al.* (1995) devoted to study a three-dimensional full-scale ten-cup combustion sector with double annular. Calculations were carried out for the same geometry and operating conditions using the CONCERT-3D CFD code. Lai (1997) modeled the inner chamber of a gas turbine combustor similar to that of the Allison 570KF turbine used by the Canadian Navy. A 22.5° periodic sector of the combustor was modeled using a structured multi-block grid. Lai included the swirled passages in his model, which was an important step in reducing the uncertainty in the boundary conditions. The simulation results for the combustor flow fields in this research did not compare with the experimental data. Gosselin *et al.* (2000) simulated steady, three-dimensional turbulent reacting flows with liquid spray, in a generic type gas turbine combustor using a hybrid structured/unstructured multi-block grid. The calculation allowed for detailed combustor geometry, including the inner chamber, external channel, and the various liner film cooling holes and dilution ports. The N-S equations were solved using the RNG turbulence model and the PDF turbulent kinetic energy reaction rate model. The calculated results for the gas temperatures, mass functions of CO/CO_2, and velocity fields were compared with experimental measurements. However, no prediction of the wall temperature was included in this work. Ho and Weng (1996) proposed a prototype simulation modeling of annular combustion chamber with two-phase flow field. Ho's research utilized the commercial code, INTERN, which was developed and technically supported by NERC. Eccles and Priddin (1999) demonstrated the capability of full-combustor structured-mesh analysis, and highlighted the usefulness of a streamlined CAD-to-grid process utilizing parametric solid models. Birkby *et al.* (2000) developed a description of an analysis of an entire industrial gas turbine combustor, in which the premixing fuel nozzle was coupled with the combustion chamber. Snyder and Stewart (2001) developed a CFD analysis on an entire PW6000 combustor domain to predict temperature distribution at the combustor exit and compared the CFD result with the full annular rig-test data.

The method for enhancing the population of distributed power system is to modify the burner of a commercial MGT from a liquid-fuel burning gas turbine system into a gas-burning one to generate the combustion power. Therefore, this numerical

simulation work serves as a preliminary study for such re-modification of burner. The corresponding simulations, aided by the commercial code CFD-ACE+, were carried out to investigate the cooling effect in a perforated combustion chamber and combustion behavior in an annular MGT when using low heating value (LHV) gas. Additionally, the thrust generated by combustion power and the temperature patterns of solid annular liners and combustor outlets were also discussed. With the aid of the constructed combustor model, the performance of a methane-used MGT can be realized before the experiment procedure starts.

2. Mathematical model

In this study, we did the simulation of steady and three-dimensional thermo-flow field inside the annular combustion chamber. The areas of the simulation included combustion chamber, fuel pipe, air inlet, and air outlet. In order to make the problem more tractable, several assumptions were made as all gaseous mixtures are regarded as the ideal gases; the flow is steady, compressible, and turbulent; properties in solid are constant; neglect the turbulence-combustion interaction and radiation heat transfer; Soret (or thermo) diffusion, accounting for the mass diffusion resulting from temperature gradients, is neglected (Kuo, 1986). Operation conditions include four different rotational speeds of compressor as 45,000, 80,000, 120,000, and 155,000. The corresponding simulated mass flow rate of fuel, at each specific rotational speed of compressor, could be divided into four mass-fraction conditions, that is, the highest one was 90 percent of methane and the lowest was 60 percent.

2.1 Domain descriptions

The MGT adopted in this study is illustrated in Figure 1(a). This MGT system is only 136 $\times$ 89 mm. It comprises five units: the compressor, diffuser, turbine, combustion chamber and casing. In this study, it is interesting in the thermo-flow fields caused by combustion behaviors resulted from the oxidation of gaseous fuel, methane. Especially, the emphases are on the heat transfer of spreading flame, heat damage of solid bodies, and thrust generated from expansion of hot gases. In order to simplify the simulation, it does not include the consideration of rotating parts. However, it retains the combustion chamber and the remaining zones, including the space in between casing and outer liner, the gap between diffuser outlet and front cover of combustion chamber, which are shown in Figure 1(b). The domain of combustion chamber consists of three major components. They are the solid annulus dual liners (inner and outer), which have several discharge holes, the fuel tube, which plays the role of fuel transportation, and the fluids, such as gas fuel and air, filling with the remaining spaces. The annulus combustor has 12 fuel tubes and the liner holes and relative components are in a periodic arrangement shown as Figure 1(b). Therefore, the combustor can be divided into 12 sub-chambers geometrically. The configuration of the three-dimensional model domain employed for simulation in this study is illustrated in Figures 1(c) and (d).

2.2 Governing equations

Based on the assumptions mentioned above, the governing equations are given as follows[1]:

Mass conservation

$$\nabla \bullet (\rho \vec{V}) = 0 \tag{1}$$

which describes the net mass flow across the control volume's boundaries is zero.

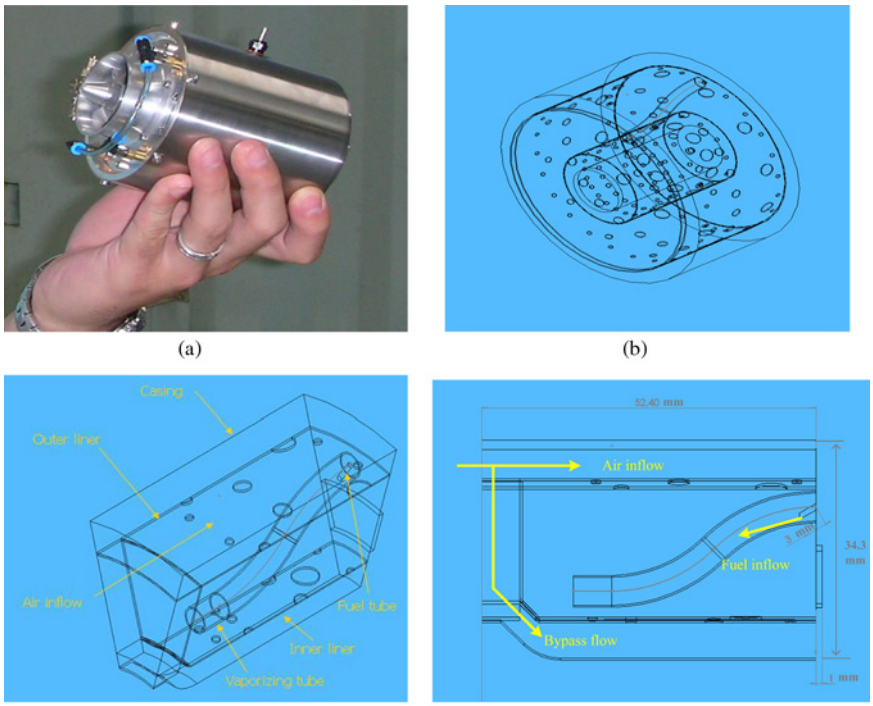

Notes: (a) Picture of annular MGT; (b) combustor chamber of MGT; (c) one-twelfth of annulus combustion chamber; and (d) the lateral view of (c)

Figure 1.
The simplifying procedure of model domain

Momentum conservation. Based on the general Newton's second law and particular viscous stress law, the momentum equations are developed as Navier-Stokes equations:

$$\frac{\partial}{\partial x_j}(\rho u_j u_i - \tau_{ij}) = -\frac{\partial p}{\partial x_i} \tag{2}$$

where u_i and u_j are the absolute fluid velocity components in directions of x_i and x_j, ρ is the density, τ_{ij} is the shear stress tensor component, and p is the pressure.

In Newtonian fluid, the viscous stresses are proportional to the deformation rates of the fluid element. The nine viscous stress components can be related to velocity gradients to produce the following shear stress terms:

$$\tau_{ij} = 2\mu s_{ij} - \frac{2}{3}\mu \frac{\partial u_k}{\partial x_k}\delta_{ij} - \overline{\rho u_i' u_j'} \tag{3}$$

$$s_{ij} = \frac{1}{2}\left(\frac{\partial u_i}{\partial x_j} + \frac{\partial u_j}{\partial x_i}\right) \tag{4}$$

where μ is the molecular dynamic fluid viscosity, δ_{ij} the "kronecker delta", which is unity when i = j and zero otherwise, s_{ij} the rate of strain tensor.

Energy conservation. Heat transfer processes are computed by energy equation in the form known as the total enthalpy equation:

$$\nabla \bullet (\rho u_i h) = \nabla \bullet (k_{eff} \nabla T) + \frac{\partial}{\partial x_j}(u_i \tau_{ij}) + S_h \tag{5}$$

where S_h are the energy sources, h is the total enthalpy. In laminar flow, this will be the thermal conductivity of the fluid, k. In turbulent flow:

$$k_{eff} = k + \frac{\mu_t C_p}{\mathrm{Pr}_t} \tag{6}$$

where Pr_t is the turbulent Prandtl number.

Species conservation

$$\frac{\partial}{\partial x_j}(\rho u_j Y_i) = \frac{\partial}{\partial x_j}\left(\rho D_i \frac{\partial Y_i}{\partial x_j}\right) + M_i \omega_i \tag{7}$$

where Y_i represents mass fraction for mixture gas of CH_4, O_2, CO_2, H_2O and inert N_2. The term $M_i \omega_i$ is the mass production rate of species. M_i is the molecular weight of i-th species. ω is global one-step reaction rate and in the Arrhenius form for methane combustion is computed as (Bui-Pham, 1992):

$$\omega = k_r Y_{CH_4} Y_{O_2} \tag{8}$$

where k_r is the reaction rate constant that can be written in the Arrhenius form as:

$$k_r = BT^{\alpha} \exp(-Ea/RT) \tag{9}$$

where B is the rate constants that pre-exponential factor, α is the temperature exponent, and Ea/R is the activation temperature.

Here one-step global reaction mechanism is adopted, the pre-exponential factor, temperature exponent and activation temperature are described as follows:

One-step global reaction mechanism

$$CH_4 + 2O_2 \rightarrow CO_2 + 2H_2O \tag{10}$$

with the reaction rate expression as:

$$\frac{d[CH_4]}{dt} = -(2.5 \times 10^{12})e - \left(\frac{24{,}355}{T}\right)[CH_4]^{0.2}[O_2]^{1.3} \tag{11}$$

The dynamic viscosity for each species is calculated using Sutherland's law (ESI Group Company). The selected values for all species are tabulated in Table I.

Table I. Sutherland's law coefficients of dynamic viscosity

Sutherland's law coefficients	Species CH_4	O_2	CO_2	H_2O	N_2
A	1.2515E-06	1.7830E-06	1.5034E-06	1.8670E-06	1.4050E-06
B	197.4	156	222.26	708	111.5

Gas thermal conductivity, k_t, is derived from Prandtl number as:

$$Pr = \frac{\mu C_p}{k_t} \tag{12}$$

In this work, Pr = 0.707 is selected.

The diffusion coefficient, D, is calculated by Schmidt number:

$$\mathrm{Sc} = \frac{\mu}{D} \tag{13}$$

In this work, Sc = 0.7 is selected. The constant properties of solid are tabulated in Table II.

Turbulent model. The Reynolds averaged Navier-Stokes simulation adopts k-ε model which involves solutions of transport equations for turbulent kinetic energy and its rate of dissipation. The model adopted here is based on the research results of Launder and Spalding which was referred in the sample model of a micro gas turbine engine in CFD-ACE+ Manual. The transport equations for the standard k-ε model are as follows:

$$\frac{\partial}{\partial t}(\rho k) + \frac{\partial}{\partial x_j}(\rho u_j k) = \rho P - \rho \varepsilon + \frac{\partial}{\partial x_j}\left[\left(\mu + \frac{\mu_t}{\sigma_k}\right)\frac{\partial k}{\partial x_j}\right] \tag{14}$$

$$\frac{\partial}{\partial t}(\rho \varepsilon) + \frac{\partial}{\partial x_j}(\rho u_j \varepsilon) = C_{\varepsilon 1}\frac{\rho P \varepsilon}{k} - C_{\varepsilon 2}\frac{\rho \varepsilon^2}{k} + \frac{\partial}{\partial x_j}\left[\left(\mu + \frac{\mu_t}{\sigma_\varepsilon}\right)\frac{\partial k}{\partial x_j}\right] \tag{15}$$

where $C_\mu = 0.09$; $C_{\varepsilon 1} = 1.44$; $C_{\varepsilon 2} = 1.92$; $\sigma_k = 1.0$; $\sigma_\varepsilon = 1.3$.

Note that the standard k-ε model is a high Reynolds model and is not intended to be used in the near-wall regions where viscous effects dominate the effects of turbulence. Instead, standard wall functions are used in cells adjacent to walls.

2.3 Boundary conditions

The settings of boundary conditions are specified within the operating range of components that are confirmed by means of the size specification through the classically thermodynamic theory. The boundary values are corresponding to different operating conditions. In the model domain, it consists of two inlets, one outlet, two physical symmetric surfaces (including one cyclic symmetric surface), interfaces between two different phases (solid and gas), and the remaining wall. The non-slip boundary conditions are applied on the solid walls. The outlet locates at the rear of combustion chamber whose function is to guide the hot gas to generate thrust power. The outlet conditions of combustion chamber mainly determined by what is happened upstream. The parameters, such as temperature, velocity, and pressure, at outlet

Material	Density (kg/m^3)	Specific heat (J/kg-K)	Thermal conductivity (W/m-K)
Stainless steel 316	8,000	500	21.5

Table II.
Properties of solid liner

boundary are assumed zero gradients there, and the flow rate in outlet boundary must satisfy with mass balance. Before numerical simulation in CFD-ACE+, the air-fuel ratio in the boundary condition had to be determined. Because this study used fuel with an LHV, the fuel-weak ratio, which is typically used for MGT engines, was not suitable for this study. Therefore, this study used a Stoichiometric to calculate the air-fuel ratio. Typically, simulation results calculated utilizing the Stoichiometric markedly affected heat transfer. This effect on heat transfer is a major disadvantage when designing a kerosene turbine engine. However, due to the characteristics of the LHV fuel in this study, the Stoichiometric was suitable. The parameter factors that were considered in this study included the fuel concentration (the mixing ratio of CH_4 and CO_2) and rotation speed of the turbine. Since the required consumption mass flow rate of mixture at fuel inlet can be derived based on stoichiometry, the air flow rate at specific rotation speed should be calculated first. What follows give an example involved with the calculation methods for setting the air inlet boundary conditions at the rotational speed 155,000 rpm and compression ratio 2.35.

Air inlet boundary conditions. Step 1: Modify compression ratio. The user manual of MGT states that the compression ratio of the Garrett compressor needs to be modified when the compressor is attached to this engine. The empirical formula for modifying compression ratio is $\pi_{\text{mod.}} = \sqrt{\pi} = 1.533$.

Step 2: Look up the corresponding value of air mass flow. With the rotation speed and the modified compression ratio, the corresponding value of air mass flow rate can be consulted from the compressor map. The value is $\dot{m} = 0.166$ (kg/s).

Step 3: Calculate the increased temperature after compressing process. Assume the ideal air gas compression process for compressor is isentropic and adiabatic, the temperature rise could be calculated through the thermodynamics formula as follows:

$$\Delta T^{\rightarrow 2}_{actual} = \frac{\Delta h^{1\rightarrow 2}_{ideal}}{C_p \cdot \eta} = \frac{T_1}{\eta}\left[\left(\frac{P_2}{P_1}\right)^{0.286} - 1\right] \tag{16}$$

where 1 represents the state at compressor inlet, 2 represents the state at compressor outlet. Thus, $T_2 = 353.3$ K is calculated as $T_1 = 298$ K.

Step 4: Calculate the air flow speed at compressor outlet. The air flow velocity $V = 70.52$ (m/s) for the outlet of compressor is derived from the equations $P_2 = \pi_{\text{mod.}}, P_1 = \rho R_u T_2$ and $\dot{m}_{air} = \rho V A$, where A is the outlet cross-section of compressor and the value is 1,545.66 (mm^2). All the inlet boundary conditions, are summarized in Table III.

Operation conditions rpm	Air inlet Hydraulic diameter (D_h) = 0.012 m, turbulence intensity (I) = 0.04, $Y_{N2} = 0.768$, $Y_{O2} = 0.232$ CR	V (m/s)	T_2 (K)	Fuel inlet $D_h = 0.001$ m, I = 0.05, T = 298 K Mass flow rate (kg/s)
155,000	2.35	70.52	353.33	7.08E-05
120,000	1.85	50.26	337.13	4.69E-05
80,000	1.35	38.03	316.68	3.23E-05
45,000	1.1	16.04	304.32	1.28E-05

Table III.
Boundary conditions of combustion chamber

3. Numerical method

In solving the Navier-Stoke equation, the semi-implicit pressure linked equation correlation (SIMPLEC) algorithm was a widely used numerical method. Different from other algorithms adopting finite difference method, this SIMPLEC adopts finite volume method. Figure 1(b) showed the model of annular combustion chamber used in the CFD-ACE. The model was developed by SolidWorks; then, it was imported to the CFD-ACE+ as IGS file. Afterwards, the mesh arrangement was accomplished by the CFD-ACE+ pre-processing, also called CFD-GEOM.

4. Grid-independence test

For obtaining the acceptable numerical solution, this work applies the unstructured tetrahedral grids produced from geometry models to carry out grid-independence test. The grid-independence tests include both cold flow and combustion cases. Because the over-heating problem of liners is one of concerns in this research, the grid densities is increased especially near the liners, whose thicknesses are only 0.4 mm, and the vaporizing tube, which is about 0.3 mm in thickness. Owing to adoption of upwind numerical difference scheme, the grid amount should be dense enough to avoid the false diffusion phenomenon. The operating conditions are specified as that the air inflow of $V = 70.52$ (m/s) is generated by compressor with a compression ratio 2.35 under the rotation rate 155,000 rpm, and the fuel tube supplies a mixing fuel of methane (mass fraction 0.8) and CO_2 (mass fraction 0.2) under a fixed mass flow rate ($\dot{m} = 7.08\text{E-}05\ \text{kg/s}$). From the above discussion, the mass flow rate, velocity, and temperature of gas mixture ejected from the rear of combustion chamber are the emphasized data. Thus the total flow amount through the liner holes of the primary zone is the major concern. Two different grid distributions (densities) are tested: One is the grid number of 446097, the other is 717974. The convergence criterion is selected as 10^{-3}, whose value is applied for all of simulations afterward. The test results are listed in Table IV. From the information given by the table, it can be seen that the maximum relative errors of various physical quantities are all less than 2 percent. To negotiate with the computational time, the grid number of 446097 is adopted in this study. Apply PC of Pentium 4 with CPU 3.0 GHz, 2 GB RAM to carry out the computation. The computational time for a typical simulation needs about 60 h.

5. Results and discussion

The flow field was analyzed with a selected cross-section at 7.5° angle from datum symmetric face illustrated as Figures 2(a) and (b). This cross-section contain at least one liner hole in each different function zone on the combustion chamber wall. The analyzed results include the distributions of temperature, CH_4 mass fraction, O_2 mass fraction, and velocity vector. Table V presented some important data of the simulation results.

	446,097grids geometry: tetrahedral grids min. size: 3.964E-014 m^3	717,974grids geometry: getrahedral grids min. size: 8.47E-015 m^3	Relative error (%)
Outlet mass flow rates (kg/s)	7.04E-03	7.02E-03	0.28
Outlet max. temperature (K)	788.7	794.7	0.76
Outlet max. velocity (z-direction) (m/s)	192.4	188.7	1.96
Average outlet velocity (z-direction) (m/s)	149.4	146.7	1.84

Table IV. Grid test results of different grid densities

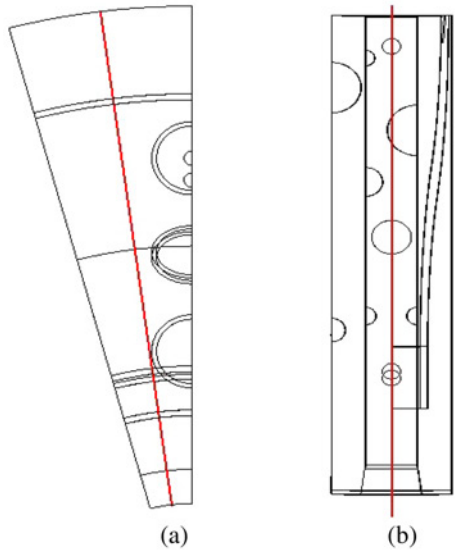

Notes: (a) Front view and (b) top view

Figure 2.
Cross-section at 7.5° (datum on symmetric face)

Rotational speed = 155,000 rpm				
Mass fraction of methane in fuel mixture	0.9	0.8	0.7	0.6
Outlet mass flow rate (kg/s)	3.21E-03	3.21E-03	3.21E-03	3.20E-03
Outlet maximum speed (z direction) (m/s)	219.1	192.4	173.2	158.9
Average thrust (N)	28.4	25.2	22.8	20.7
Average outlet mass flow rate of CO_2 (kg/s)	1.74E-04	1.48E-04	1.29E-04	1.17E-04
Average outlet mass flow rate of H_2O (kg/s)	1.28E-04	9.72E-05	7.39E-05	5.76E-05
Rotational speed = 120,000 rpm				
Mass fraction of methane in fuel mixture	0.9	0.8	0.7	0.6
Outlet mass flow rate (kg/s)	4.67E-03	4.66E-03	4.66E-03	4.65E-03
Outlet maximum speed (z direction) (m/s)	162.6	142	127.3	116.6
Average thrust (N)	13.9	12.2	11	9.9
Average outlet mass flow rate of CO_2 (kg/s)	1.14E-04	9.71E-05	8.45E-05	7.70E-05
Average outlet mass flow rate of H_2O (kg/s)	8.39E-05	6.36E-05	4.84E-05	3.78E-05
Rotational speed = 80,000 rpm				
Mass fraction of methane in fuel mixture	0.9	0.8	0.7	0.6
Outlet mass flow rate (kg/s)	3.21E-03	3.21E-03	3.21E-03	3.20E-03
Outlet maximum speed (z direction) (m/s)	128.2	111.5	99.5	91.7
Average thrust (N)	7.5	6.6	5.9	5.4
Average outlet mass flow rate of CO_2 (kg/s)	7.85E-05	6.69E-05	5.82E-05	5.39E-05
Average outlet mass flow rate of H_2O (kg/s)	5.78E-05	4.38E-05	3.33E-05	2.65E-05
Rotational speed = 45,000 rpm				
Mass fraction of methane in fuel mixture	0.9	0.8	0.7	0.6
Outlet mass flow rate (kg/s)	1.27E-03	1.27E-03	1.27E-03	1.27E-03
Outlet maximum speed (z direction) (m/s)	54.9	48	43	39.5
Average thrust (N)	1.3	1.1	1	0.9
Average outlet mass flow rate of CO_2 (kg/s)	3.04E-05	2.63E-05	2.33E-05	2.09E-05
Average outlet mass flow rate of H_2O (kg/s)	2.24E-05	1.72E-05	1.34E-05	1.03E-05

Table V.
Simulation results at different rotation speed

Figure 3 shows the simulation result of temperature distribution in the annular MGT system with different concentration of CH_4; it demonstrated that with the proper value of air-fuel ratio, the temperature inside the core of annular combustion chamber was as high as 2,200 K. This represented that combustion did exist inside the combustion chamber. The traditional turbine engine usually had swirling mechanism to increase recirculating. The recirculating could assist fluid mixing and hold the combustion flame. The simulation result shown in Figure 3 demonstrated that although the annular combustion chamber in this study did not have swirling mechanism, the design still created a proper recirculating zone to concentrate the flame at the center of the chamber, and prevent the flame from expanding to cause hot spot. The other phenomenon shown in Figure 3 was that the cool air flows via dilution holes on liners were fully functional. A sufficient turbulence must be promoted in the dilution zone so that the hot and cold streams are thoroughly mixed to give the desire output temperature distribution, with no hot streaks which could damage the turbine wheel. The jet flow demonstrated in Figure 3, which discharged from dilution holes, cooled down the exhaust gas temperature effectively. The average exhaust temperature of combustor outlet was below the endurance temperature 700 °C. The simulation result shown in Figure 4 demonstrated the distribution of CH_4 mass fractions in primary zone. It was realized that the fuel supply system could deliver the fuel properly to ensure that the combustion reaction occurred at the front of the combustion chamber. In Figure 4, the CH_4 mass fraction in primary zone increase with CH_4 concentration rising. Moreover, larger CH_4 mass fraction produces much more severe reaction at interface zero methane mass fraction and mass diffusion zone of methane concentration gradient. When the function of intermediate holes was discussed, Figure 5 shows the distribution of O_2 mass fraction with different

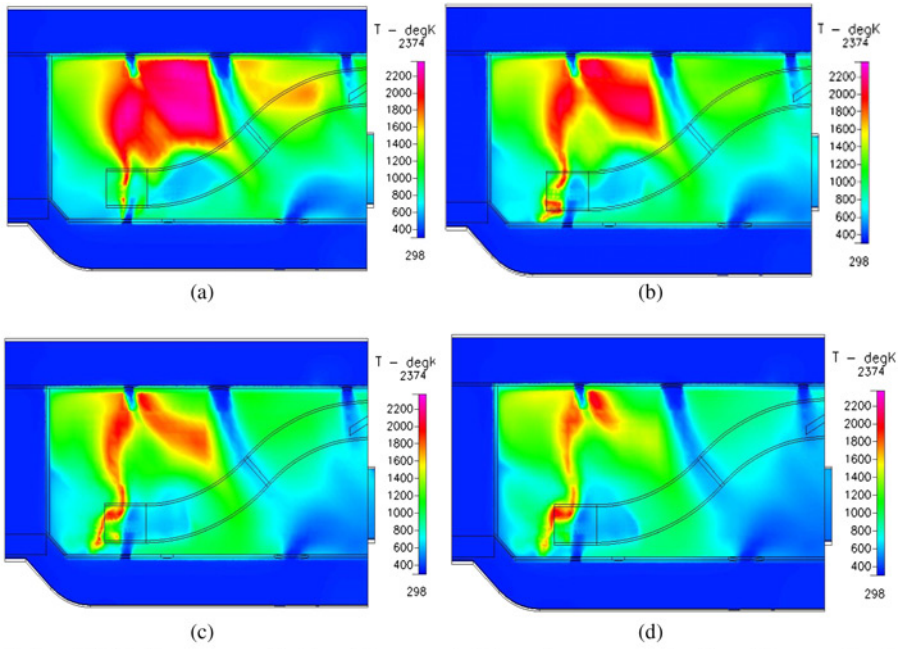

Notes: (a) Methane concentration, 90 percent; (b) methane concentration, 80 percent; (c) methane concentration, 70 percent; and (d) methane concentration, 60 percent

Figure 3.
Distributions of temperature for 155,000 rpm

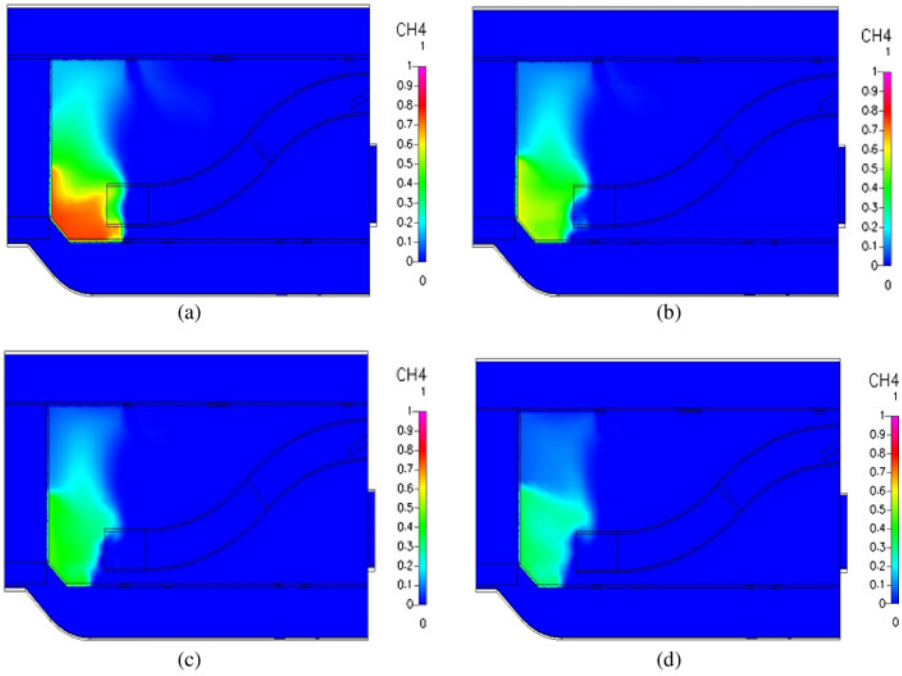

Figure 4.
Distributions of CH_4 mass fraction for 155,000 rpm

Notes: (a) Methane concentration, 90 percent; (b) methane concentration, 80 percent; (c) methane concentration, 70 percent; and (d) methane concentration, 60 percent

concentration of CH_4 and indicated that large number of compressed air was induced to the combustion chamber via the intermediate holes. Under this condition, combustion would be done more completely and less dissociated product would occur. Figure 6 shows the combustor outlet velocity magnitude. In addition, the distributions of exhausting velocity at outlet were not uniform. The distributions of velocity vector inside combustor were complicated as a result of mutual influence of jets flow discharged from liner holes. The flow paths and directions between outer liner wall and fuel tube roughly induced toward the outer liner wall.

The combustor outlet, which is next to the turbine, emits high-temperature gas. The critical endurance temperature of the turbine blade is roughly 700 °C (973 K). Figure 7 shows simulation results for maximum temperature at the combustor outlet. In each case, outlet temperature increased as methane mass fraction increased. When 90 percent methane fuel was employed, no prediction exceeded the maximum temperature the turbine wheel can tolerate. The numerical results show that, among these simulation conditions, heat damage to the turbine blade was less than that to liners. One reasons is that the outlet of chamber is far from the solid zones of the liners; thus, and then the outlet of chamber experiences minimal over-heating problem as mentioned maximum previously. The other reason is that cool airflows via the liner dilution holes are fully functional. The jet flow discharged from dilution holes cool the exhaust gas effectively. Figure 8 shows the average exhaust temperatures at the combustor outlet. All temperatures are far below the endurance temperature of 700 °C. The simulation results mentioned above explain that turbine blades would incur heat damage locally not totally when methane mass fraction unity occurs.

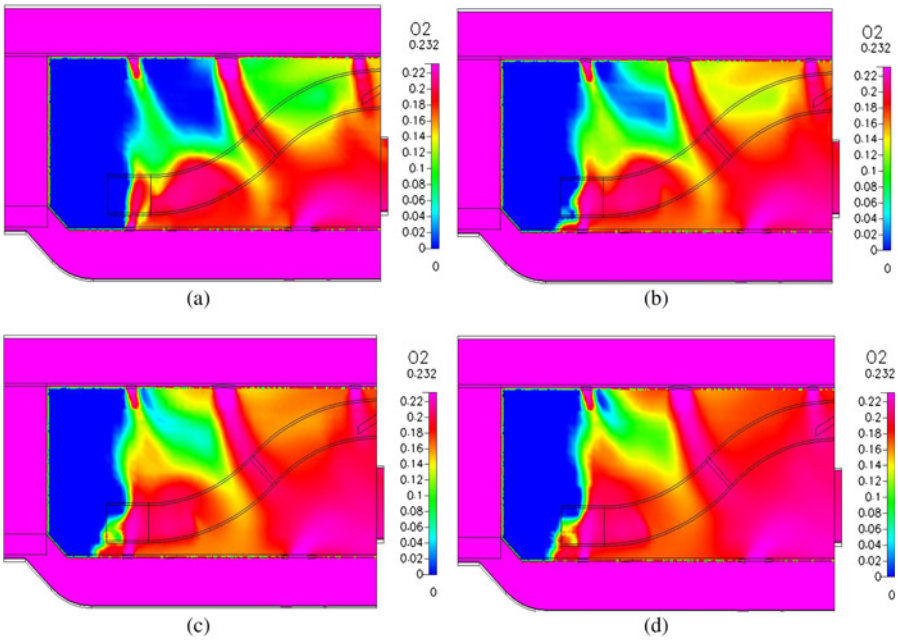

Notes: (a) Methane concentration, 90 percent; (b) methane concentration, 80 percent; (c) methane concentration, 70 percent; and (d) methane concentration, 60 percent

Figure 5.
Distributions of O_2 mass fraction for 155,000 rpm

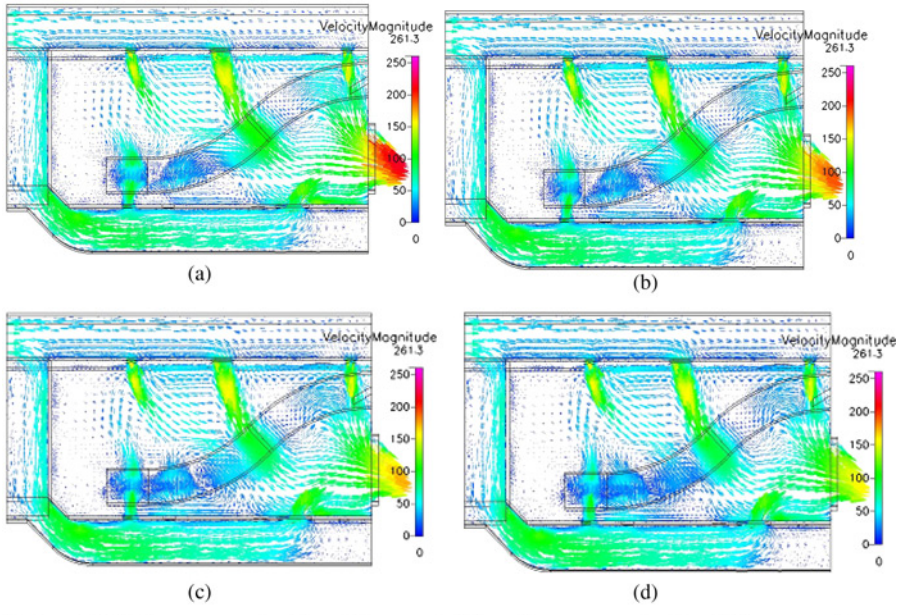

Notes: (a) Methane concentration, 90 percent; (b) methane concentration, 80 percent; (c) methane concentration, 70 percent; and (d) methane concentration, 60 percent

Figure 6.
Velocity vector of flow field for 155,000 rpm

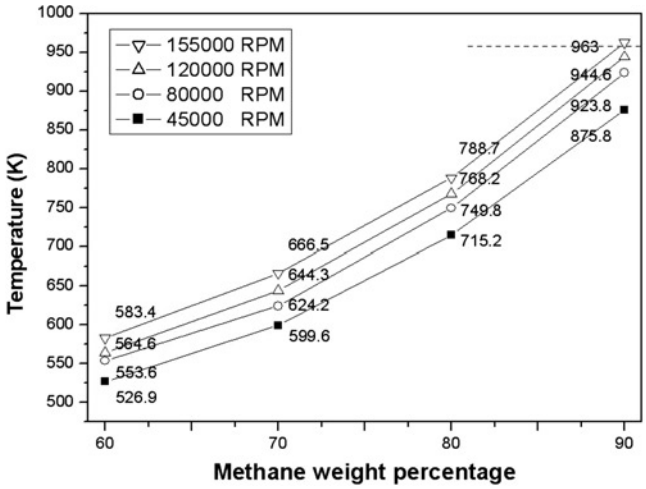

Figure 7.
Maximum temperature of combustor outlet

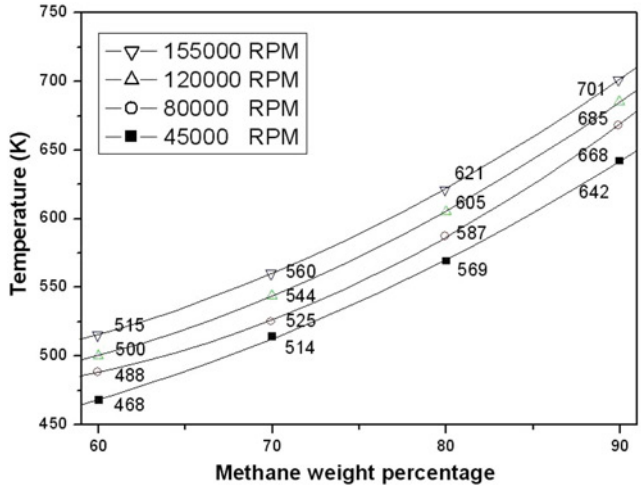

Figure 8.
Average temperature of combustor outlet

The CO_2 gas emitted from the combustor causes the environmental pollution. Recently developed methods for recycling or absorbing CO_2 through bio-chemical procedures are feasible. Table V lists the average outlet CO_2 and H_2O mass flow rates for future reference. As the methane mass fraction increased, the CO_2 and H_2O mass flow rates increased. These numerical simulation results were expected. Additionally, for the case of 80,000 rpm with 90 percent methane, the CO_2 mass flow rate (7.85E-05) was larger than that of H_2O (5.78E-05). Based on equation $CH_4 + 2O_2 \rightarrow 2H_2O + CO_2$, the stoichiometric clearly confirms output results.

When designing a combustion chamber, hot spots must be prevented as they would burn through the combustion chamber and cause the engine to fail. Figure 9 shows the maximum temperatures on liner walls. A combustor wall made of stainless steel 316 must be capable of tolerating high temperatures. The maximum temperature is roughly 900 °C (1,173 K); therefore, most liners under simulated conditions (which were above the

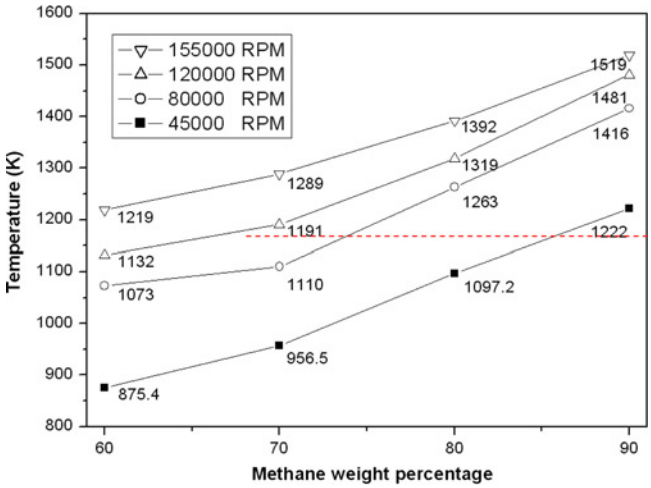

Figure 9.
Maximum temperature on liners of combustor

grey dotted line in Figure 9) burned out. Figure 10(a)-(d) shows the simulation results of the temperature distribution on the solid surface at 155,000 rpm under different mass percentages of methane. The overheated points were located at the outer liners. The size of the high-temperature areas on the outer liners increased as methane mass fraction increased; moreover, the highest temperatures gradually moved toward the intermediate zone of the outer liners when the methane mass fraction increased. Thus, the phenomenon of overheating was unlikely as the heating value of methane is lower than that of Jet A1 fuel and the original combustor design for Jet A1 fuel does not cause heat damage to liners. The possible reasons for above phenomena are as follows. First, the simulation lacked appropriate data for physical properties of solid stainless steel 316. Both thermal conductivity and specific heat employed in the simulation for the solid liner were measured at low temperatures. However, at 900 °C, these parameters are uncertain. Based on thermodynamics, $\Delta H \approx C_p \Delta T$, and heat conduction theory, $\dot{q} = k\Delta T = h_{coef}.\Delta T$, the increase in specific heat C_p and heat conduction decrease ΔT when heat flux and enthalpy variation are fixed. The above phenomenon could cause the decreasing of temperature increasing difference from a cold flow to combustion on liners. Both C_p and k increased as temperature increased. Hence, using smaller value to these variables would cause over-prediction of liner temperature. Second, the simulation employed a fixed setting for turbulent Prandtl and Schmidt numbers everywhere in the combustor. The turbulent Prandtl and Schmidt numbers were 0.7 for the CFD model. This relatively low value may agree with the condition when the combustor is mixing fuel and air. However, the relatively low values for Prandtl and Schmidt numbers increased the heat transfer rate compared to that using a higher value. Since the convective heat transfer rate is increased on both sides of the liner, the effect of heat transfer on wall temperature was relatively small. The temperature gradient through the wall, however, was over-predicted (Bui-Pham, 1992). Third, the internal flow fields were changed by methane gas. The process of transportation and consumption for liquid Jet A1 fuel is as follows. The liquid Jet A1 fuel absorbs latent heat generated by vaporization when it passes through the vaporizing tube. The liquid Jet A1 fuel gradually transforms into gas fuel. The gas fuel combines with oxygen in air to start the combustion reaction. Compared with liquid Jet A1 fuel, methane has a single-phase transportation process. Additionally, the energy

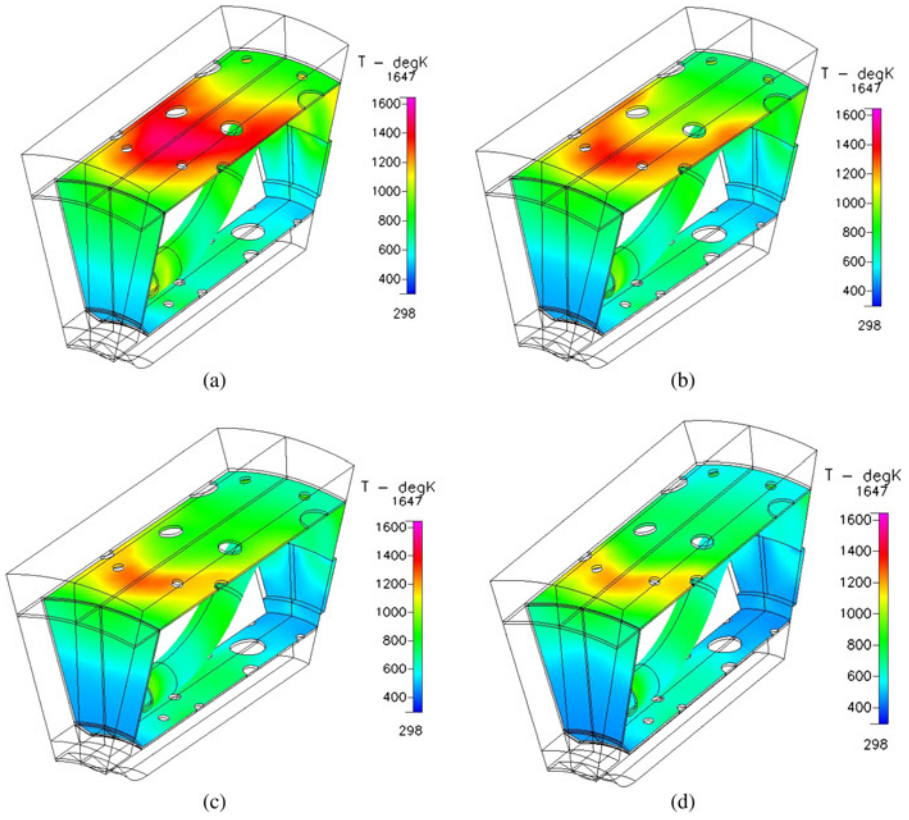

Figure 10.
Temperature distributions on solid liners and fuel tube

Notes: (a) Methane concentration, 100 percent; (b) methane concentration, 90 percent; (c) methane concentration, 80 percent; and (d) methane concentration, 70 percent

density of methane is smaller than that of Jet A1 fuel, which increases the flow rate of fuel for consumption. These changes can generate very different flow fields. The simulation results show that the maximum thrust generated by methane fuel is 28.4 N (Table V). However, the thrust is calculated from combustion outlet. It is different from the real thrust calculated from nozzle outlet; hence, we cannot compare the data with the engine instruction manual demonstrating that the maximum thrust generated by Jet A1 fuel is 44 N. The temperature distribution in depth of the outer liner was conducted by the heat transfer among three zones: combustion gas flow, air flow comes from the compressor, and the solid outer liner in between. Figure 11 shows the temperature distribution on the line probe and corresponding positions. The line probe is on a symmetrical face. The end points are on wall edges of the vaporizing tube and at half depth of the outer annual flow channel. The liner temperature gradient across the liner is small (outer liner, 1,301 K; inner liner, 1,320 K) because the liner is thin (0.4 mm). However, the two side flows adjacent to the outer liner wall have sharp temperature gradients due to the relatively poor heat transfer effects on the solid liner.

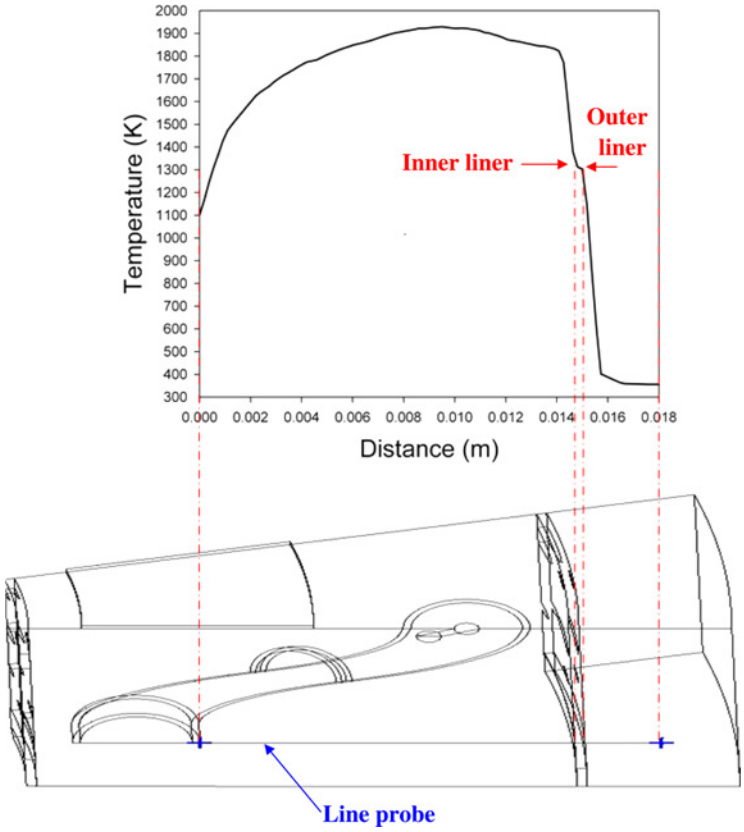

Figure 11.
Temperature distribution on line probe on symmetric face

6. Conclusions and future works

The numerical simulation model of methane-used annular MGT engine with three-dimensional flow field was built. This numerical model provided designers of MGT engine with a reliable guidance. The proposed system in this study reduces the size of a distributed power supply system for biogas (methane) and enhances its popularization. This miniature power supply system is suited to household power use after it attaches a generator. The results are summarized as follows:

- The liners temperature may be estimated unreasonable because it lacks appropriate data of specific heat and heat conductivity for stainless-steel liner at high temperature. In addition, fixed constant setting of turbulent Prandtl and Schmidt numbers would cause liner over heat.
- The function of dilution holes is maintained. Although the fuel is changed into methane gas, the hot gas exhausted from combustor outlet is cooled down by jet flow effectively.

Based on the above-mentioned conclusions and drawbacks, here some recommendations are addressed for possible solutions.

- Join compressor and turbine with combustor to complete the coupled fluid-solid simulation. In order to get more real physical mechanism, the coupled fluid-solid

simulation should take into consideration. Moreover, adding nozzle guide vanes and nozzle to accomplish real thrust calculating, which helps comparing thrust generated by Jet A1 fuel.

- Improve the one-step chemical reaction model to four steps. The reason to recommend four-step reaction model is that it includes the oxidation of substance CO, which is also a fuel. In many textbooks, the jet flow discharged from intermediate zone of liner is designed for recovering the dissociation losses of CO. In addition, the exhaust of CO is an issue of environment protection. Moreover, the difference of total reaction rates between one step and four steps may result in different level of heat accumulation in combustor. Thus, more phenomena can be studied by using four-step chemical reactions.

Note

1. ESI Group Company, *CFD-ACE+ V2004 Modules Manual V1*.

References

Birkby, P., Cant, R.S. and Dawes, W.N. (2000), "CFD analysis of a complete industry lean premixed gas turbine combustor", *ASME Proceedings*, Paper-0131.

Bui Pham, M.N. (1992), "Studies in structures of laminar hydrocarbon flames", PhD dissertation, University of California, San Diego, CA.

Eccles, N.C. and Priddin, C.H. (1999), "Accelerated combustor design using CFD", *Proceedings of the 14th Conference, Florence University, Florence, Italy, 11 September, ISABE*, Paper-7094.

Gosselin, P., DeChamplain, S., Kalla, and Kretschmer, D. (2000), "Three-dimensional CFD analysis of a gas turbine combustor", *Proceedings of the 36th AIAA Joint Propulsion Conference and Exhibition, Huntsville, AL*.

Gulati, A., Tolpadi, A.K., Vandeusen, G. and Burrus, D.L. (1995), "Effect of dilution air on scalar flowfield at combustor sector exit", *Journal of Propulsion Power*, Vol. 11, pp. 1162-9.

Ho, W.C. and Weng, L.C. (1996), "Annular combustor for miniature jet engine", *International Journal of Turbo and Jet Engines*, pp. 105-15.

Kuo, K.K. (1986), *Principles of Combustion*, John Wiley & Sons, Toronto.

Lai, M.K. (1997), "CFD analysis of liquid spray combustion in a gas turbine combustor", *Proceedings of the International Gas Turbine and Aeroengine Congress and Exposition, Orlando, FL*.

Snyder, T.S. and Stewart, J.F. (2001), "Application of an advanced CFD-based analysis system to PW6000 combustor to optimize exit temperature distribution", *Proceedings of the ASME International Mechanical Engrg. Congress and Exposition, 11-16 November, New York, NY*, Paper-0064.

Corresponding author

Chun-Hsiang Yang can be contacted at: seanyang.me93g@nctu.edu.tw